Bridging NiCo layered double hydroxides and Ni_3S_2 for bifunctional electrocatalysts: the role of vertical graphene

Xiao Zhang,[a] Jiajun Fan,[a] Xunyu Lu,[b] Zhaojun Han,[*b,c,d] Claudio Cazorla[e], Long Hu[a], Tom Wu[a] and Dewei Chu[*a]

[a]*School of Materials Science and Engineering, UNSW Sydney, NSW 2052, Australia. E-mail: d.chu@unsw.edu.au*

[b]*School of Chemical Engineering, UNSW Sydney, NSW 2052, Australia. E-mail: zhaojun.han@unsw.edu.au*

[c]*School of Mechanical and Manufacturing Engineering, UNSW Sydney, NSW 2052, Australia*

[d]*CSIRO Manufacturing, 36 Bradfield Road, Lindfield, NSW 2070, Australia*

[e]*Department of Physics, Polytechnic University of Catalonia (UPC), C/ Jordi Girona 1-3, Campus Nord, B4-203 08034 Barcelona (Spain)*

Abstract

In this work, we report a bifunctional electrocatalyst with nickel sulphide (Ni_3S_2) as the template, vertical graphene (VG) as the bridging material, and nickel-cobalt layered double hydroxides (NiCo LDHs) nanosheets as the active catalyst. The hybrid Ni_3S_2/VG@NiCo LDHs catalyst exhibits excellent activity in alkaline solution for both OER (overpotential ~320 mV at a current density of 100 mA cm^{-2}) and HER (overpotential ~120 mV at a current density of 10 mA cm^{-2}). In addition, the hybrid catalyst possesses superior stability with 99% retention of voltage upon a continued current density of 20 mV cm^{-2} for over 24 hours. It is found that the transitions of Ni^{2+}/Ni^{3+} and Co^{2+}/Co^{3+} ions enable excellent HER and OER performances, and VG bridging between NiCo LDHs and Ni_3S_2, enable fast charge-transfer and a high density of active sites, resulting in the improved electrical conductivity, intrinsic activity, and electrochemical stability. This work provides a guideline to design the architecture of bifunctional catalysts for highly efficient water splitting applications.

Introduction

Electrochemical water splitting driven by renewable power such as solar and wind is a promising method to produce high-purity and sustainable hydrogen.[1] Thermodynamically, water splitting is a very energy-unfavourable process, where expensive noble-based metals are often used to overcome the energy barrier of reactions.[2] To reduce the cost, it is thus essential to develop earth-abundant, highly active and stable catalysts for both hydrogen evolution reaction (HER) and oxygen evolution reaction (OER), the two half-reactions in electrochemical water splitting, so as to enable widespread industrial applications.[3]

Despite much effort, it is still challenging to achieve highly-efficient water splitting using non-noble metal-based electrocatalysts for both half-reactions. This is due to several roadblocks. First, water splitting is often conducted in either strong acidic or alkaline environments to maximize the ion transport,[4] which is harsh for earth-abundant metal catalysts as they usually become unstable or inactive.[5] Second, different equipment and processes are required to produce stable catalysts for HER and OER, which could raise the fabrication cost and the associated hydrogen production cost.[6] Lastly, OER catalysts are usually more active in alkaline and neutral solutions than in acidic solution, whereas HER catalysts often behave oppositely with better performance in acidic solution.[7] To address these issues, bifunctional hybrid catalysts have recently received large interests as they can effectively drive both HER and OER in the same solution.[8]

Among the bifunctional catalysts, nickel-based two-dimensional (2D) layered double hydroxides (LDHs) have shown promising electrochemical activity.[9] For instance, NiCo CoMn, and NiFe LDHs have been found as one of the best OER catalysts in the alkaline solution owing to their abundant active sites.[10] [11]In addition, the expansion of nanosheets during oxidation process can facilitate the anion exchange.[12] However, Ni-based LDHs materials suffer from the intrinsic drawback of low electrical conductivity. Nickel sulphides

(*e.g.*, NiS, NiS_2, and Ni_3S_2), on the other hand, show an intrinsic metallic behaviour with high electrical conductivity. It has been considered as a very promising material to fabricate bifunctional hybrid catalysts for water splitting.[13] Nevertheless, the electrocatalytic activity of nickel sulphides is still far lower than that of noble metal materials.[14] To enhance the electrocatalytic performance of bifunctional catalysts, two approaches are often implemented: (i) increasing the intrinsic activity of each active site (*e.g.*, using morphological tuning[15]) and (ii) increasing the number of active sites (*e.g.*, introducing the intercalating ions[16]). In many cases, the two approaches are used concurrently in order to achieve the best performance.[17]

Herein, we report a hybrid electrocatalyst which combines the high catalytic activity of NiCo LDHs and high electrical conductivity of Ni_3S_2, bridged by vertical graphene (VG). VG possesses a unique morphology of graphene nanosheets aligned perpendicularly to the substrate surface with an interconnected porosity. VG is directly grown on Ni_3S_2 foam formed by pre-sulphide treatment of Ni foam, followed by electrodeposition of NiCo LDHs. The vertical orientation, interconnected porosity and high electrical conductivity of VG ensure fast ion and charge transports in the hybrid electrocatalyst.[18] Furthermore, both VG and NiCo LDHs share a similar layered structure, which helps to optimize the potential of 2D heterostructures through synergistic effects.[19] As such, the Ni_3S_2/VG@NiCo LDHs hybrid electrodes exhibit a profoundly high overall water splitting performance, outperforming the state-of-the-art IrO_2 benchmark in OER and demonstrating competitive activity toward the state-of-the-art Pt/C benchmark in HER. Therefore, the key innovation in this work is the combination of high performance OER catalyst (NiCo LDH) and HER catalyst (Ni_3S_2) through the bridging of vertical graphene, which enables bi-functional catalysis with high activity and stability. We attribute the high performance of bifunctional catalysts mainly to (i) fast charge transfer facilitated by good electrical conductivity of Ni_3S_2 and VG, and (ii) increased

electrocatalytically active areas by the porous thin nanosheets structure of VG and NiCo LDHs.[20],[21]

2. Experimental section

2.1. Chemicals and materials

Cobalt(II) nitrate hexahydrate ($Co(NO_3)_2•6H_2O$, M_w: 182.94), nickel(II) nitrate hexahydrate ($Ni(NO_3)_2•6H_2O$, M_w: 290.81), sulphur powder, toluene (C_7H_8, M_W: 92.14), urea (CH_4N_2O, M_w: 60.04), potassium hydroxide (KOH, M_w: 56.11), ethanol (C_2H_6OH, M_w: 46.07), methane (CH_4, M_W: 16.043) and nickel foam (420 g m^{-2}) were purchased from Sigma-Aldrich and used without further purification.

2.2. Ni_3S_2 foam

Nickel sulphide (Ni_3S_2) on nickel foam (NF) was synthesized *via* a hydrothermal method. Briefly, a 2 x 1 cm^2 NF was soaked in 6 M HCl for 15 minutes to remove the surface native oxide layer, followed by washing with ethanol and deionized water, and dried at room temperature. 50 mg sulphur powder was dissolved into 30 mL toluene under ultrasonication, which was then transferred into a 50 mL Teflon-lined stainless-steel autoclave. A piece of pre-cleaned NF was immersed into the solution and heated to 150 °C for 5 hours. Finally, the Ni_3S_2/NF was washed with ethanol and dried at room temperature under vacuum.

2.3. Synthesis of VG

VG was directly grown on substrates (bare NF and Ni_3S_2/NF) by plasma-enhanced chemical vapor deposition (PECVD).[22] Briefly, the substrate was firstly loaded into a vacuum chamber. Ar gas was then flowed at a rate of 10 sccm when the chamber pressure achieved a pressure of 2 x 10^{-2} Pa. Next, Ar plasms was ignited by a 13.56 MHz radio-frequency (RF) power source

at 1,000 W, with H_2 and CH_4 gases introduced at 10 and 20 sccm respectively. The temperature was raised to ~400 °C under the plasma without additional heating. Finally, VG was obtained after 10 min growth at a height of 5 – 10 μm.

2.4. Synthesis of NiCo LDHs

The NiCo LDHs were synthesized *via* electrodeposition using the three-electrode configuration. Four substrates were used as the working electrode, *namely*, bare NF, NF/VG, NF/Ni_3S_2 and NF/Ni_3S_2/VG. The working electrode was placed in a 100 mL solution of 4 mM $Ni(NO_3)_2$•$6H_2O$ and 1.3 mM $Co(NO_3)_2$•$6H_2O$ with Pt foil as the counter electrode and Ag/AgCl as the reference electrode. The solution was kept in cold water bath at 10 °C, and the working voltage was held at -1 V for 45 minutes. The electrode was then rinsed with deionized water and dried in vacuum chamber at room temperature. Four heterostructure electrodes were obtained, *i.e.,* bare NF with NiCo LDHs (Ni@NiCo LDHs), NF/VG with NiCo LDHs (Ni/VG@NiCo LDHs), sulfurized NF with NiCo LDHs (Ni_3S_2@NiCo LDHs) and sulfurized NF/VG with NiCo LDHs (Ni_3S_2/VG@NiCo LDHs).

2.5. Materials characterization

Crystalline structural analysis of the as-synthesized samples was determined by using an X-ray diffraction (MPD PANalytical Xpert multipurpose X-ray diffraction system using filtered Cu Kα radiation, λ = 0.1541 nm). The microstructure and morphology were characterized by scanning electron microscopy (SEM; FEI Nova SEM 450) operated at 20 kV e-beam and transmission electron microscopy (TEM; FEI Philips Tecnai CM200) operated at 200 kV e-beam. Raman spectra were obtained by using a Renishaw inVia 2R Raman spectrometer at laser excitation of 514 nm. The surface elements composition and chemical bonding states were

determined by energy dispersive spectroscopy (EDS; FEI Nova SEM 450) under 15 kV e-beam and X-ray photoelectron spectroscopy (XPS; ESCALAB250Xi spectrometer).

2.6. Electrochemical tests

All electrochemical tests were performed in 1 M KOH aqueous electrolyte without *iR* compensation. Linear sweep voltammograms (LSV) and cyclic voltammograms (CV) were obtained by an electrochemical workstation (CHI604E, CH Instruments Inc.). In a three-electrode configuration, the as-fabricated electrodes were used as working electrodes, Pt foil as the counter electrode, and Ag/AgCl as the reference electrode. The applied potential was calibrated and converted to reversible hydrogen electrode (RHE) by $E_{RHE} = E_{Ag/AgCl} + 0.197 + 0.059 \times pH$. For the LSVs, OER and HER were measured from 0 to 0.8 V and -0.9 V to -1.5 V vs Ag/AgCl, respectively, at a scan rate of 5 mV s^{-1}. Electrochemical impedance spectroscopy (EIS) and chronoamperometric measurements were recorded by an Autolab electrochemical workstation (PGSTAT302N). The EIS were measured at frequency ranging from 100 kHz to 0.1 Hz at an overpotential of 300 mV. The charge transfer resistance (R_{ct}) was estimated from the equivalent circuit of Nyquist plots. R_s meant the solution resistance and it was a constant value because of the same electrolyte used (1 M KOH). Chronoamperometric measurements were obtained at a constant current density of 20 mA cm^{-2} for 24 hours. Tafel slopes were calculated according to the equation $\eta = a + b\ log(j)$, where η is the overpotential, j defines the current density, and a and b are the constants.[23] Lastly, electrochemically active surface areas (ECSAs) were determined from the electrochemical double-layer capacitance (C_{dl}) by analysing CV curves under the potential ranging from 100 mV to 150 mV at different scan rates of 5, 10, 20, 40 ,60, 80, 100 mV/s. The measured current in this non-Faradic potential region should be mostly due to the charging of the double-layer. By plotting the capacitive currents ($\Delta j = j_a - j_c$) against the scan rate and following with a linear fit, C_{dl} is around half of

the slope. The ESCA can be estimated from C_{dl} according to Ni = C_{dl} / C_s, where C_s is the specific capacitance of a flat surface with 1 cm^2 of geometric surface area. Here we used 40 μF cm^{-2} as the standard for the ECSA estimation.

3. Results and discussion

3.1. Morphology and structure of NiCo LDHs

NiCo LDHs were electrodeposited through the reduction of nitrates from the solution of $Ni(NO_3)_2$ and $Co(NO_3)_2$, as schematically illustrated in Fig. 1. The morphology of the samples is shown in Fig. 2, where Figs. 2a and 2b show SEM images of pristine VG and VG@NiCo LDHs grown on Ni_3S_2, respectively. The images clearly indicate that VG has been successfully deposited on the NF/Ni_3S_2. The thickness and size of the VG nanosheets are measured in a range of 1 – 5 nm and 50 – 500 nm, respectively, which agree well with the previous studies.[24] After the electrodeposition, NiCo LDHs are uniformly coated on VG (Fig. 2b), maintaining the loosely porous structure of VG. This unique feature is mainly attributed to the extremely long and thin edges of VG, which contain exposed carbon atoms with unsatisfied valence states as the nucleation sites for the deposition of NiCo LDHs, known as "reactive edges".[25] These reactive edges bound strongly with NiCo LDHs and provided fast electron transport channel as "bridging materials". The microstructure was further analysed by TEM. Fig. 2c shows a cluster of graphene nanosheet covered by NiCo LDHs. From the high-resolution TEM images, the lattice spacing of 0.33 nm indicates the (0 0 2) graphitic plane of VG (Fig. 2d), while those of 0.24 nm and 0.28 nm correspond to the (1 1 1) and (0 2 1) planes of Ni_3S_2 respectively (Fig. 2e). Moreover, the lattice spacing of NiCo LDHs was measured after fast Fourier transform (FFT) processing, where 0.294 nm and 0.26 nm represent the (1 0 1) and (2 2 1) planes of the NiCo LDHs respectively (Fig. 2f).

Raman spectra show typical graphene peaks at ~1350, ~1580, ~2650 and ~2800 cm^{-1}, corresponding to the disordered D, the graphitic G, the 2D and the disorder D + graphitic G (D+G) bands, respectively (Fig. S1).[26] The ratio of peak intensity is also studied to reveal the defects and crystalline structure of VG. The I_D/I_G decreased from 1.32 to 1.28 while I_{2D}/I_G decrease from 0.67 to 0.61 in the presence of Ni_3S_2. These calculations suggested that less defects are presented in the final hybrid Ni_3S_2/VG@NiCo LDHs electrodes. Two minor peaks are also observed at ~550 and ~1100 cm^{-1} in the lower band range of Ni_3S_2/VG@NiCo LDHs, which can be ascribed to the NiCo LDHs and S-OH respectively. In addition, Fig. 3a shows the XRD patterns of Ni_3S_2/VG@NiCo LDHs, in which the peaks could be well indexed to the heazlewoodite phase of Ni_3S_2 (ICSD no. 98-002-3114) and the NiCo LDHs (JCPDS no. 48-0083).[27] The diffraction peaks at 44.5° and 51.8° arose from the metallic Ni (ICSD no. 01-071-3740). As no additional peaks belonging to NiS or NiS_2 are found, the surface Ni foam was thus sulfurized to Ni_3S_2.

The XPS scan was also carried out to study the chemical states of Ni_3S_2/VG@NiCo LDHs. The composition of as-obtained hybrid Ni_3S_2/VG@NiCo LDHs electrode included Ni, Co, C and S elements, which can be clearly identified in Fig. S2. In the Ni 2p XPS spectrum (Fig. 3b), the peaks with binding energies (BEs) of 855.1 eV and 872.6 eV are attributed to Ni^{2+}, and the peaks at BEs of 857.5 eV and 874.6 eV are characteristics of Ni^{3+}.[28] The weak peak at the BEs of 853.5 eV is the ascribed to the Ni-S bond, which further confirms the successful sulphuration and is also consistent with previous reports.[29] The Co 2p (Fig. 3c) spectrum show typical $2p_{3/2}$ and $2p_{1/2}$ doublets due to the spin-orbit coupling in transition metals. Two valence states for Co are found, with the deconvoluted peak at 781 eV ascribed to the Co^{2+} state of α-$Co(OH)_2$ and the peaks at 780.3 eV and 797 eV to Co^{2+} in β-$Co(OH)_2$ and Co^{3+} in CoO(OH) respectively.[30] As a result, Ni and Co possess multiple valence states in the NiCo LDHs. The O 1s region in Fig. 3d can be deconvoluted into three peaks: the peaks at

529.5 eV is from metal-oxygen bonding; the peak located at 531.2 eV is ascribed to OH^- from NiCo LDHs; and the peak at 532.5 eV is from the absorbed oxygen.[31] The results of EDS mapping shown in Fig. S3 further confirm the existence of the electrodeposited NiCo LDHs bridged by VG.

3.2. OER catalytic performance

The OER catalytic performance of electrodes was obtained in O_2-saturated 1 M KOH aqueous solution using a three-electrode configuration. Four as-prepared electrodes, Ni@NiCo LDHs, Ni/VG@NiCo LDHs, Ni_3S_2@NiCo LDHs and Ni_3S_2/VG@NiCo LDHs, were tested as the working electrode, with Pt foil and Ag/AgCl as the counter and reference electrodes respectively. The pristine VG and Ni_3S_2 layers were also tested in the same configuration as the controls.

The LSV curves in Figs. 4a and 4b show that as compared to the Ni@NiCo LDHs and Ni_3S_2@NiCo LDHs, the Ni/VG@NiCo LDHs have a small onset potential (~ 1.52 V). It also shows a low overpotential (430 mV) at a current density of 100 mA cm^{-2}. Furthermore, by introducing the Ni_3S_2 layer as the base for VG and NiCo LDHs, the Ni_3S_2/VG@NiCo LDHs demonstrate the best catalytic performance among all samples, reaching the smallest onset potential of 1.48 V and the lowest overpotential of 350 mV at a current density of 100 mA cm^{-2}. Such performance is not only competitive than that of the state-of-the-art transition metal hydroxides and oxyhydroxides anchored on carbon-based electrocatalysts[32], such as NiFe LDH@DG (240 mV @ 10 mA/cm^2), ultrathin CoNi LDHs (70 mV @ 10 mA/cm^2 with iR correction) and $Ni_{0.5}Co_{0.5}$-9AC-AD (350 mV @ 10 mA/cm^2 with iR correction) (see Table S1), but also outperforming the commercial IrO_2 which exhibited a overpotential of 580 mV at a current density of 100 mA/cm^2 in 1 M KOH electrolyte (Fig. S4).[33] The oxidation peak at about 1.4 V is due to the oxidation of Ni bivalent to trivalent to form NiOOH.[34] It has been

confirmed that the catalytically active site of the Ni-based catalyst is located in the structure of NiOOH during the OER process.[35] The results demonstrate the number of oxidation-active Ni atoms is correlated with the Ni_3S_2 performance, although the peroxidation peaks (Fig. 4a) may also contribute to the lowering of overpotential. Furthermore, the corresponding Tafel plots are shown in Fig. 4c, where the transfer pattern is determined based on whether it is a one-step or multiple-step process. Ni_3S_2/VG@NiCo LDHs show more favourable kinetics towards the OER with a low Tafel slope of 65 mV dec^{-1}, outperforming that of Ni@NiCo LDHs (114 mV dec^{-1}), Ni/VG@NiCo LDHs (89 mV dec^{-1}), and Ni_3S_2@NiCo LDHs (97 mV dec^{-1}).

The stability test of Ni_3S_2/VG@NiCo LDHs was carried out at a constant current density of 20 mA cm^{-1} (Fig. 4d). The results indicate that the catalyst retained 99% of the original potential after 24 hours, which demonstrates excellent durability of the catalyst. To study the resistance of electron transfer from catalyst to electrolyte, the EIS of NiCo LDHs were measured (Fig. 4e). The value of charge transfer resistance (R_{ct}) was obtained by fitting and simulating the EIS data into an equivalent circuit (inset of Fig. 4e). The R_{ct} values are determined to be 20.5, 55.3, 120 and 270 Ω for the Ni_3S_2/VG@NiCo LDHs, Ni/VG@NiCo LDHs, Ni_3S_2@NiCo LDHs, and Ni@NiCo LDHs, respectively. Clearly, the Ni_3S_2/VG@NiCo LDHs electrode shows the smallest R_{ct} among all samples, suggesting the excellent electrical conductivity of VG as bridging materials which could contribute to faster OER kinetics. Lastly, the double-layer capacitance (C_{dl}) was plotted to estimate the ECSA of Ni_3S_2/VG@NiCo LDHs by cyclic voltammograms in the non-Faradic region (Fig. S5). The Ni_3S_2/VG@NiCo LDHs possess a value of C_{dl} at 21.3 mF cm^{-2}, which is larger than that of Ni/VG@NiCo LDHs (15.8 mF cm^{-2}), Ni_3S_2@NiCo LDHs (11.08 mF cm^{-2}), and Ni@NiCo LDHs (11.6 mF cm^{-2}). The electrodes with VG thus provided more active sites due to the porous structure and large surface area of VG.

3.3. HER catalytic performance

Apart from the OER performance, the HER activity of NiCo LDHs was also investigated in the same three-electrode configuration in 1.0 M KOH electrolyte. As shown in Fig. 5a, Ni_3S_2/VG@NiCo LDHs shows the highest HER activities with the smallest onset potential of 75 mV, which is lower than those of Ni/VG@NiCo LDHs (80 mV), Ni_3S_2@NiCo LDHs (95 mV), and Ni@NiCo LDHs (117mV). Furthermore, the HER performance of Ni_3S_2/VG@NiCo LDHs is close to that of the commercial Pt/C benchmark catalyst, as shown in Fig. S6.[36] At a current density of 10 mA cm^{-2}, the overpotential of Ni_3S_2/VG@NiCo LDHs, Ni/VG@NiCo LDHs, Ni_3S_2@NiCo LDHs and Ni@NiCo LDHs are determined to be 120, 152, 175 and 240 mV, respectively (Fig. 5b). Such a value is also substantially smaller than that of the recent advances Co_9S_8 nanowires (168 mV@10 mA cm^{-2}), $Ni_{0.5}Co_{0.5}$-9AC-AD (144 mV@10 mA cm^{-2}) and 3D N, S-rGO/WSe_2/NiFe-LDH (123 mV@ 10 mA cm^{-2}) in alkaline solutions (see Table S2). Moreover, the Tafel slopes are plotted in Fig. 5c, where the Ni_3S_2/VG@NiCo LDHs exhibit the lowest slope of 87 mV dec^{-1} among Ni/VG@NiCo LDHs (98 mV dec^{-1}), Ni_3S_2@NiCo LDHs (120 mV dec^{-1}) and Ni@NiCo LDHs (132 mV dec^{-1}). The reaction pathway of HER can be roughly determined by the values of Tafel slopes. It is known that in general, there are three steps in the HER process, the Volmer step, the Heyrovsky step and the Tafel step,[37]

$M + H_2O + e^- = M\text{-}H_{ads} + OH^-$ (Volmer reaction, 120 mV dec^{-1}),

$M\text{-}H_{ads} + H_2O + e^- = M + H_2 + OH^-$ (Heyrovsky reaction, 40 mV dec^{-1}),

$M\text{-}H_{ads} = 2M + H_2$ (Tafel reaction, 30 mV dec^{-1}).

The relatively small Tafel slope of Ni_3S_2/VG@NiCo LDHs implied that the HER process is mainly promoted by the Volmer-Heyrovsky pathway. It has been demonstrated that NiCo LDHs could easily absorb H^+.[38] Combining with the fast charge transfer arising from

electrically conductive Ni_3S_2 and VG bridging material, the NiCo LDHs can effectively decompose water into H^+ and OH^-, leading to fast reaction kinetics in alkaline solution. In addition, the stability of Ni_3S_2/VG@NiCo LDHs is also superior, which can retain 98 % of the initial potential after 24 hours when tested under a constant current density of 20 mA cm^{-2} (Fig. 5d).

To gain further insights on the charge transfer between catalyst and electrolyte, EIS measurements were conducted at an overpotential of 150 mV. The Nyquist plots and the equivalent circuit model are shown in Fig. 5e, with the R_{ct} of Ni_3S_2/VG@NiCo LDHs estimated to be 14 **Ω**, which is significantly smaller than that of Ni/VG@NiCo LDHs (48 **Ω**), Ni_3S_2@NiCo LDHs (108 **Ω**) and Ni@NiCo LDHs (248 **Ω**). The small value of R_{ct} confirms that VG could enhance the electrical conductivity by bridging the two components and accelerating the electron transfer from catalyst to electrolyte. In addition, the C_{dl} is examined to verify the ECSA. The Ni_3S_2/VG@NiCo LDHs have C_{dl} of 19.3 mF cm^{-2}, which is larger than that of Ni/VG@NiCo LDHs (14.9 mF cm^{-2}), Ni_3S_2@NiCo LDHs (11.03 mF cm^{-2}), and Ni@NiCo LDHs (10.8 mF cm^{-2}). These results are consistent with those obtained in OER, corroborating that the porous structure of VG could contribute to more active sites in the NiCo LDHs.

3.4. Overall water splitting performance

Based on the above OER and HER results, we believe that the bifunctional Ni_3S_2/VG@NiCo LDHs catalyst could lead to excellent overall water splitting in alkaline solution. To verify this, we firstly evaluated the long-term stability by comparing the LSV curves before and after 1,000 CV cycles (Fig. S7). It can be seen that for both OER and HER the two curves were very close to each other, suggesting a superior stability. The morphological changes before and after the stability tests are also shown in Fig. S8. Compared to the as-prepared Ni_3S_2/VG@NiCo LDHs

(Fig. S8a), it is noticed that NiCo LDHs turned into a dense layered structure with increased thickness after the long-term OER test (Fig. S8b). This morphological change agreed well with the reported OER-active hydroxide/oxyhydroxide structure where the transformation occurred due to the phase cycling of metal hydroxide/oxyhydroxide during the oxidation.[39] In contrast, the morphology of Ni_3S_2/VG@NiCo LDHs is similar to that of the as-prepared counterpart after the long-term HER test, maintaining the porous structure of VG with little aggregation (Fig. S8c). The XPS spectra of Ni_3S_2/VG@NiCo LDHs after cycling were also obtained (Figs. S8d – S8f). It is found that the oxidation peaks of Ni 2p remained unchanged, while an obvious shift (~0.6 eV) of Co 2p towards the lower BEs (Fig. S8e) is observed after OER. Combining with the minor peak shift (~0.2 eV) in the O 1s spectra (Fig. S8f), we then conclude that the CoOOH species were formed.[40] Therefore, it could be expected that the oxidation state of Co after OER would be close to 3+. It is reasonably expected that the redox couple of Co^{2+}/Co^{3+} in the NiCo LDHs may provide a notable electrochemical activity, as Co^{3+} cations have been considered as the catalytically active centres for OER.[41]

Next, we assembled an overall water splitting cell consisting of both anode and cathode made of the Ni_3S_2/VG@NiCo LDHs. Other pairs of electrodes made of Ni_3S_2@NiCo LDHs and Pt/C||IrO_2 were also tested as controls. As shown in Fig. 6a, Ni_3S_2/VG@NiCo LDHs deliver a cell voltage of 1.66 V at a current density of 10 mA cm^{-2} in 1 M KOH alkaline electrolyte, which is close to that of the commercial Pt/C||IrO_2 cell (1.56 V).[42] Meanwhile, the Ni_3S_2@NiCo LDHs catalyst, which is in the absence of VG bridging materials, only achieved a cell voltage of 1.78 V at the same current density. The Ni_3S_2/VG@NiCo LDHs are also found to be comparable or better than other recent bifunctional catalysts for overall water splitting in alkaline media, such as Co_9S_8 nanowires@NiCo LDHs (1.63 V@10 mA cm^{-2}), FeCoNi in graphene layer (1.68 V@10 mA cm^{-2}), and other hybrid electrocatalysts (see Table S3).[43]

The long-term stability of overall water splitting was also examined in 1 M KOH at a high current density of 20 mA cm^{-2} (Fig. 6b). As seen, the overall water splitting performance of Ni_3S_2/VG@NiCo LDHs is highly stable for over 24 hours. It is therefore concluded that the Ni_3S_2/VG@NiCo LDHs bifunctional catalysts with advantageous features of large surface area, good electrical conductivity and good stability could pave the way for highly-efficient overall water splitting.

The turnover frequency (TOF) was calculated to verify the role of vertical graphene. The TOF values for Ni_3S_2/VG@NiCo LDHs could be calculated using $j \times A / (Z \times F \times m)$, where j is the current density of the catalyst at a certain overpotential, A is the geometric area of the electrode (1 cm^2), Z is the number of electrons transferred (Z = 4 for OER and Z = 2 for HER), F is the Faraday constant (96,485.33 C mol^{-1}), and m is the amount of moles of NiCo LDHs deposited (7.25 μM). By assuming all the metal loaded during the electrodeposition process acted as active sites, we can get lower-limit TOF values of 141 h^{-1} at an overpotential of 400 mV for OER and 172 h^{-1} at an overpotential of 200 mV for HER. These values are notably larger than those of NiCo LDHs deposited without Ni_3S_2 or VG.

Conclusions

In summary, a bifunctional catalytic material which consists of NiCo LDHs and Ni_3S_2 bridged by vertical graphene was fabricated as an efficient and stable electrocatalyst for overall water splitting in alkaline media. By introducing vertical graphene as the bridging material, both OER and HER catalytic performance show notable improvements. The catalyst also show excellent stability in the alkaline environment for 24 hours. The corresponding two-electrode water electrolyser using Ni_3S_2/VG@NiCo LDHs as both anode and cathode achieved a current

density of 10 mA cm^{-2} at a cell voltage of 1.66 V. This work thus provides a practically efficient approach for designing bifunctional electrocatalysts for overall water splitting.

Acknowledgement

This research was partially supported by funding from the UNSW Digital Grid Futures Institute, UNSW, Sydney, under a cross disciplinary fund scheme.

References

[1] aM. Dresselhaus, I. Thomas, *Nature* **2001**, *414*, 332-337; bJ. A. Turner, *Science* **2004**, *305*, 972-974.

[2] aM. G. Walter, E. L. Warren, J. R. McKone, S. W. Boettcher, Q. Mi, E. A. Santori, N. S. Lewis, *Chem. Rev.* **2010**, *110*, 6446-6473; bN. S. Lewis, D. G. Nocera, *Proc. Natl. Acad. Sci. U.S.A.* **2006**, *103*, 15729-15735.

[3] Y. Jiao, Y. Zheng, M. Jaroniec, S. Z. Qiao, *Chem. Soc. Rev.* **2015**, *44*, 2060-2086.

[4] E. A. Hernández-Pagán, N. M. Vargas-Barbosa, T. Wang, Y. Zhao, E. S. Smotkin, T. E. Mallouk, *Energy Environ. Sci.* **2012**, *5*, 7582-7589.

[5] C. Tang, N. Cheng, Z. Pu, W. Xing, X. Sun, *Angew. Chem. Int. Ed.* **2015**, *54*, 9351-9355.

[6] aM. S. Burke, M. G. Kast, L. Trotochaud, A. M. Smith, S. W. Boettcher, *J. Am. Chem. Soc.* **2015**, *137*, 3638-3648; bK. Zeng, D. Zhang, *Prog. Energy Combust. Sci.* **2010**, *36*, 307-326.

[7] aJ. Durst, A. Siebel, C. Simon, F. Hasche, J. Herranz, H. Gasteiger, *Energy Environ. Sci.* **2014**, *7*, 2255-2260; bC. Xia, H. Liang, J. Zhu, U. Schwingenschlögl, H. N. Alshareef, *Adv. Energy Mater.* **2017**, *7*, 1602089.

[8] aR. Gao, H. Zhang, D. Yan, *Nano Energy* **2017**, *31*, 90-95; bR. Gao, Q. Dai, F. Du, D. Yan, L. Dai, *J. Am. Chem. Soc.* **2019**, *141*, 11658-11666.

[9] aM. Shao, F. Ning, J. Zhao, M. Wei, D. G. Evans, X. Duan, *Adv. Funct. Mater.* **2013**, *23*, 3513-3518; bK. Yan, G. Wu, W. Jin, *Energy Technol.* **2016**, *4*, 354-368.

[10] L. Trotochaud, S. L. Young, J. K. Ranney, S. W. Boettcher, *J. Am. Chem. Soc.* **2014**, *136*, 6744-6753.

[11] aM. Arif, G. Yasin, M. Shakeel, X. Fang, R. Gao, S. Ji, D. Yan, *Chemistry–An Asian Journal* **2018**, *13*, 1045-1052; bW. Ye, Y. Yang, M. Arif, S. Yang, X. Fang, M. A. Mushtaq, X. Chen, D. Yan, *ACS Sustainable Chem. Eng.* **2020**, *8*, 15946-15952; cM. Arif, G. Yasin, L. Luo, W. Ye, M. A. Mushtaq, X. Fang, X. Xiang, S. Ji, D. Yan, *Appl. Catal., B* **2020**, *265*, 118559.

[12] aB. M. Hunter, H. B. Gray, A. M. Muller, *Chem. Rev.* **2016**, *116*, 14120-14136; bS. Sirisomboonchai, S. Li, A. Yoshida, X. Li, C. Samart, A. Abudula, G. Guan, *ACS Sustainable Chemistry & Engineering* **2018**, *7*, 2327-2334.

[13] aZ. Cui, Y. Ge, H. Chu, R. Baines, P. Dong, J. Tang, Y. Yang, P. M. Ajayan, M. Ye, J. Shen, *JJ. Mater. Chem. A* **2017**, *5*, 1595-1602; bL. Ren, C. Wang, W. Li, R. Dong, H. Sun, N. Liu, B. Geng, *Electrochim. Acta* **2019**.

[14] aJ. J. Lv, J. Zhao, H. Fang, L. P. Jiang, L. L. Li, J. Ma, J. J. Zhu, *Small* **2017**, *13*, 1700264; bL.-L. Feng, G. Yu, Y. Wu, G.-D. Li, H. Li, Y. Sun, T. Asefa, W. Chen, X. Zou, *J. Am. Chem. Soc.* **2015**, *137*, 14023-14026.

[15] H. Y. Wang, Y. Y. Hsu, R. Chen, T. S. Chan, H. M. Chen, B. Liu, *Adv. Energy Mater.* **2015**, *5*, 1500091.

[16] aM. S. Burke, L. J. Enman, A. S. Batchellor, S. Zou, S. W. Boettcher, *Chem. Mater.* **2015**, *27*, 7549-7558; bM. S. Burke, M. G. Kast, L. Trotochaud, A. M. Smith, S. W. Boettcher, *J. Am. Chem. Soc.* **2015**, *137*, 3638-3648.

[17] Z. W. Seh, J. Kibsgaard, C. F. Dickens, I. Chorkendorff, J. K. Nørskov, T. F. Jaramillo, *Science* **2017**, *355*.

[18] H. Wang, H. S. Casalongue, Y. Liang, H. Dai, *J. Am. Chem. Soc.* **2010**, *132*, 7472-7477.

[19] aY. Sun, S. Gao, F. Lei, Y. Xie, *Chem. Soc. Rev.* **2015**, *44*, 623-636; bA. K. Geim, I. V. Grigorieva, *Nature* **2013**, *499*, 419-425; cM. Jahan, Z. Liu, K. P. Loh, *Adv. Funct. Mater.* **2013**, *23*, 5363-5372; dY. Hou, T. Huang, Z. Wen, S. Mao, S. Cui, J. Chen, *Adv. Energy Mater.* **2014**, *4*, 1400337; eH. x. Zhong, J. Wang, Y. w. Zhang, W. l. Xu, W. Xing, D. Xu, Y. f. Zhang, X. b. Zhang, *Angew. Chem. Int. Ed.* **2014**, *53*, 14235-14239.

[20] aH. Kang, Y. Kim, S. Cheon, G.-R. Yi, J. H. Cho, *ACS Appl. Mater. Interfaces* **2017**, *9*, 30779-30785; bJ. H. Seo, I. Hwang, H. D. Um, S. Lee, K. Lee, J. Park, H. Shin, T. H. Kwon, S. J. Kang, K. Seo, *Adv. Mater.* **2017**, *29*, 1701479.

[21] L. Li, K. S. Hui, K. N. Hui, T. Zhang, J. Fu, Y.-R. Cho, *Chem. Eng. J.* **2018**, *348*, 338-349.

[22] J. R. Miller, R. Outlaw, B. Holloway, *Science* **2010**, *329*, 1637-1639.

[23] K. Fominykh, P. Chernev, I. Zaharieva, J. Sicklinger, G. Stefanic, M. Döblinger, A. Müller, A. Pokharel, S. Böcklein, C. Scheu, *ACS Nano* **2015**, *9*, 5180-5188.
[24] D. H. Seo, S. Yick, D. Su, G. Wang, Z. J. Han, K. K. Ostrikov, *Carbon* **2015**, *91*, 386-394.
[25] Z. Bo, S. Mao, Z. J. Han, K. Cen, J. Chen, K. K. Ostrikov, *Chem. Soc. Rev.* **2015**, *44*, 2108-2121.
[26] J. Shin, A. Waheed, W. A. Winkenwerder, H.-W. Kim, K. Agapiou, R. A. Jones, G. S. Hwang, J. G. Ekerdt, *Thin Solid Films* **2007**, *515*, 5298-5307.
[27] J. Yang, C. Yu, X. Fan, J. Qiu, *Adv. Energy Mater.* **2014**, *4*, 1400761.
[28] aJ. Jiang, A. Zhang, L. Li, L. Ai, *J. Power Sources.* **2015**, *278*, 445-451; bJ. Bao, X. Zhang, B. Fan, J. Zhang, M. Zhou, W. Yang, X. Hu, H. Wang, B. Pan, Y. Xie, *Angew. Chem.* **2015**, *127*, 7507-7512.
[29] aJ. Li, J. Li, Z. Ding, X. Zhang, Y. Li, T. Lu, Y. Yao, W. Mai, L. Pan, *Chem. Eng. J* **2019**, *378*, 122108; bH. Du, R. Kong, F. Qu, L. Lu, *Chem. Commun.* **2018**, *54*, 10100-10103.
[30] aT. A. Mulinari, F. A. La Porta, J. Andrés, M. Cilense, J. A. Varela, E. Longo, *CrystEngComm* **2013**, *15*, 7443-7449; bJ. Yang, H. Liu, W. N. Martens, R. L. Frost, *The Journal of Physical Chemistry C* **2010**, *114*, 111-119.
[31] aY. Shao, Y. Zhao, H. Li, C. Xu, *ACS Appl. Mater. Interfaces.* **2016**, *8*, 35368-35376; bJ. Sun, W. Li, B. Zhang, G. Li, L. Jiang, Z. Chen, R. Zou, J. Hu, *Nano Energy* **2014**, *4*, 56-64; cK. Zhou, W. Zhou, L. Yang, J. Lu, S. Cheng, W. Mai, Z. Tang, L. Li, S. Chen, *Adv. Funct. Mater.* **2015**, *25*, 7530-7538.
[32] aW. Ye, Y. Yang, X. Fang, M. Arif, X. Chen, D. Yan, *ACS Sustainable Chemistry & Engineering* **2019**, *7*, 18085-18092; bR. Gao, D. Yan, *Nano Research* **2018**, *11*, 1883-1894.
[33] Y. Pan, Y. Wu, H. A. Hsain, R. Su, C. Cazorla, D. Chu, *J. Mater. Chem. A* **2020**, *8*, 13437-13442.
[34] aX. Li, G.-Q. Han, Y.-R. Liu, B. Dong, W.-H. Hu, X. Shang, Y.-M. Chai, C.-G. Liu, *ACS Appl. Mater. Interfaces.* **2016**, *8*, 20057-20066; bB. Dong, K.-L. Yan, Z.-Z. Liu, J.-Q. Chi, W.-K. Gao, J.-H. Lin, F.-N. Dai, Y.-M. Chai, C.-G. Liu, *J. Electrochem. Soc.* **2018**, *165*, H102.
[35] O. Diaz-Morales, D. Ferrus-Suspedra, M. T. Koper, *Chem. Sci.* **2016**, *7*, 2639-2645.
[36] N. Song, S. Hong, M. Xiao, Y. Zuo, E. Jiang, C. Li, H. Dong, *J. Colloid Interface Sci.* **2020**.
[37] C. Di Giovanni, W.-A. Wang, S. Nowak, J.-M. Grenèche, H. l. n. Lecoq, L. Mouton, M. Giraud, C. d. Tard, *ACS Catal.* **2014**, *4*, 681-687.
[38] aJ. Greeley, T. F. Jaramillo, J. Bonde, I. Chorkendorff, J. K. Nørskov, *Nat. Mater.* **2006**, *5*, 909-913; bW. Sheng, M. Myint, J. G. Chen, Y. Yan, *Energy Environ. Sci.* **2013**, *6*, 1509-1512.
[39] aM. Gao, W. Sheng, Z. Zhuang, Q. Fang, S. Gu, J. Jiang, Y. Yan, *J. Am. Chem. Soc.* **2014**, *136*, 7077-7084; bF. Song, X. Hu, *Nat. Commun.* **2014**, *5*, 1-9.
[40] N. McIntyre, M. Cook, *Anal. Chem.* **1975**, *47*, 2208-2213.
[41] aY. Li, P. Hasin, Y. Wu, *Adv. Mater.* **2010**, *22*, 1926-1929; bM. W. Kanan, J. Yano, Y. Surendranath, M. Dinca, V. K. Yachandra, D. G. Nocera, *J. Am. Chem. Soc.* **2010**, *132*, 13692-13701.
[42] C. Huang, T. Ouyang, Y. Zou, N. Li, Z.-Q. Liu, *J. Mater. Chem. A* **2018**, *6*, 7420-7427.
[43] aJ. Yan, L. Chen, X. Liang, *Sci. Bull.* **2019**, *64*, 158-165; bY. Yang, Z. Lin, S. Gao, J. Su, Z. Lun, G. Xia, J. Chen, R. Zhang, Q. Chen, *ACS Catal.* **2016**, *7*, 469-479.

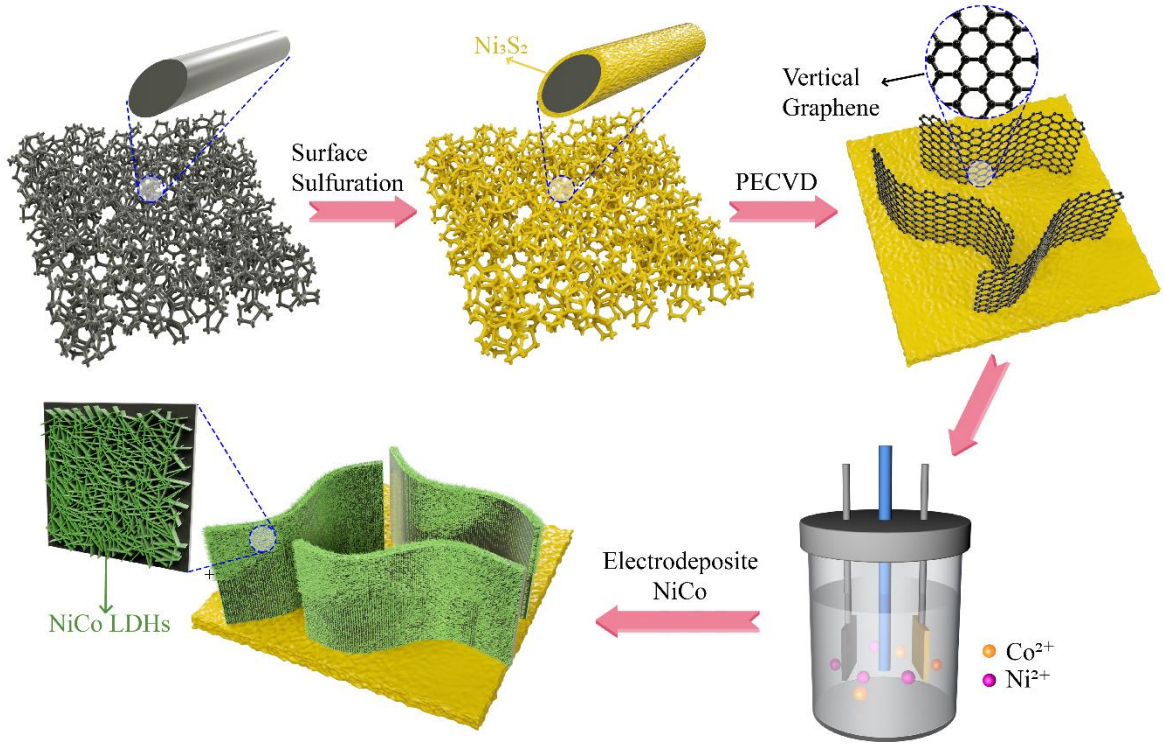

Fig. 1 Schematic illustration of the synthesis of Ni_3S_2/VG@NiCo LDHs.

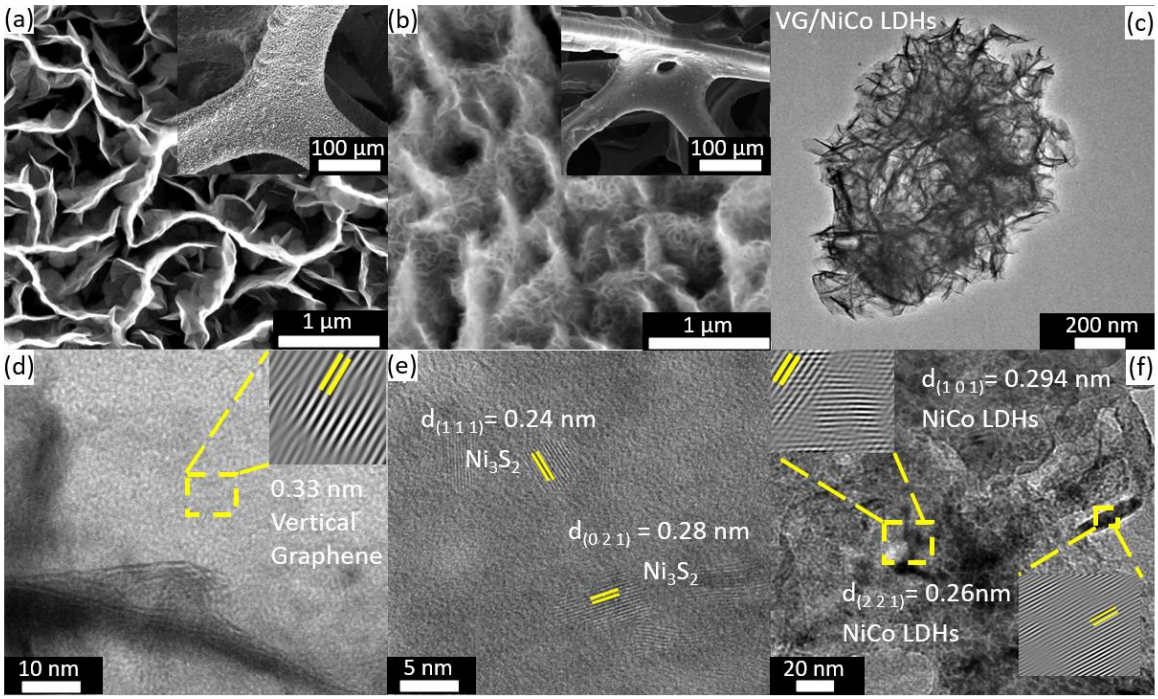

Fig. 2 (a-b) SEM images of Ni_3S_2/VG and Ni_3S_2/VG@NiCo LDHs. The insets are the low-resolution images. (c) Low-resolution TEM image of Ni_3S_2/VG@NiCo LDHs. (d-f) High-resolution TEM images of VG, Ni_3S_2, and NiCo LDHs.

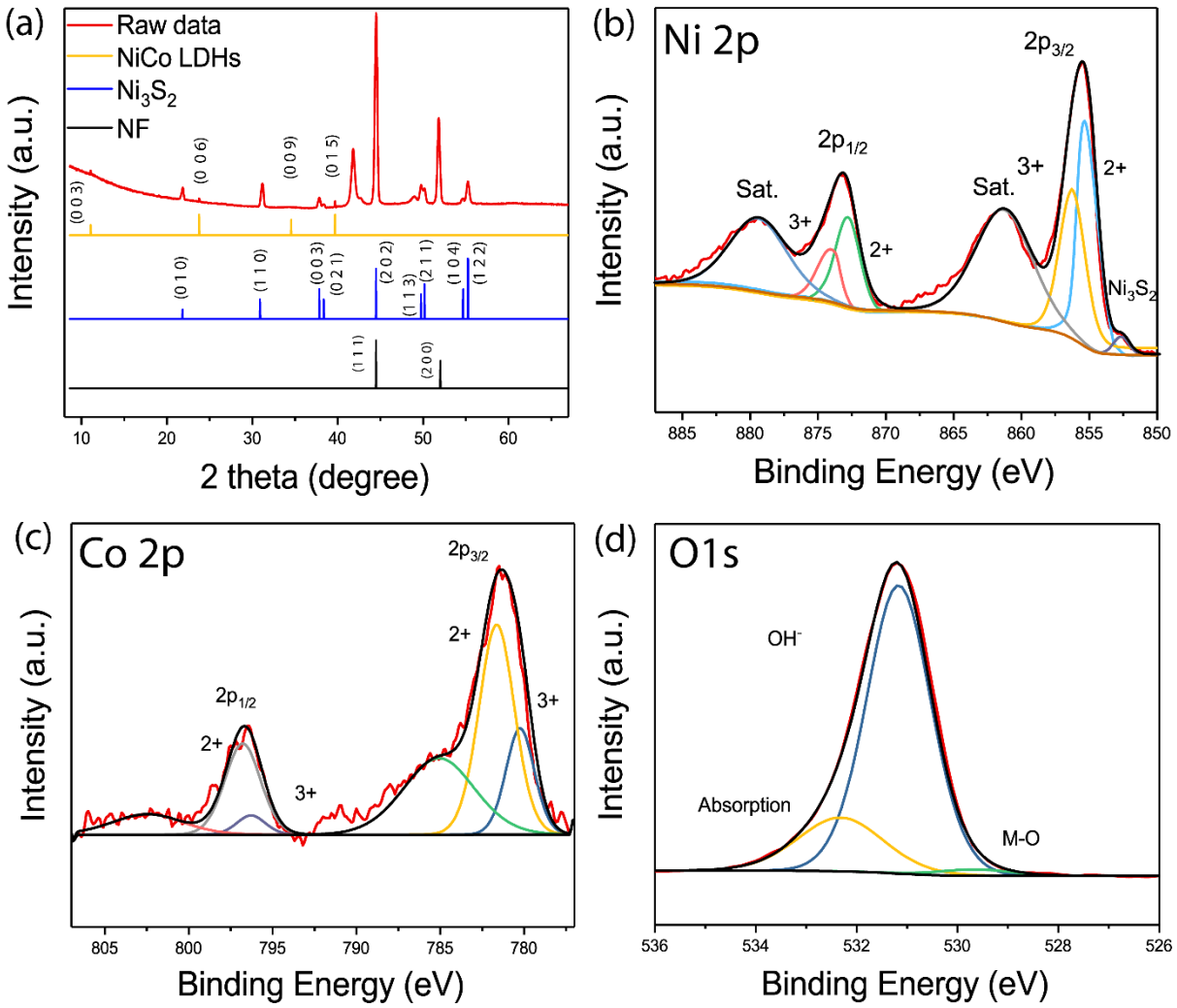

Fig. 3 (a) XRD patterns of Ni_3S_2/VG@NiCo LDHs. (b-d) XPS spectra of O 1s, Ni 2p, and Co 2p of the Ni_3S_2/VG@NiCo LDHs.

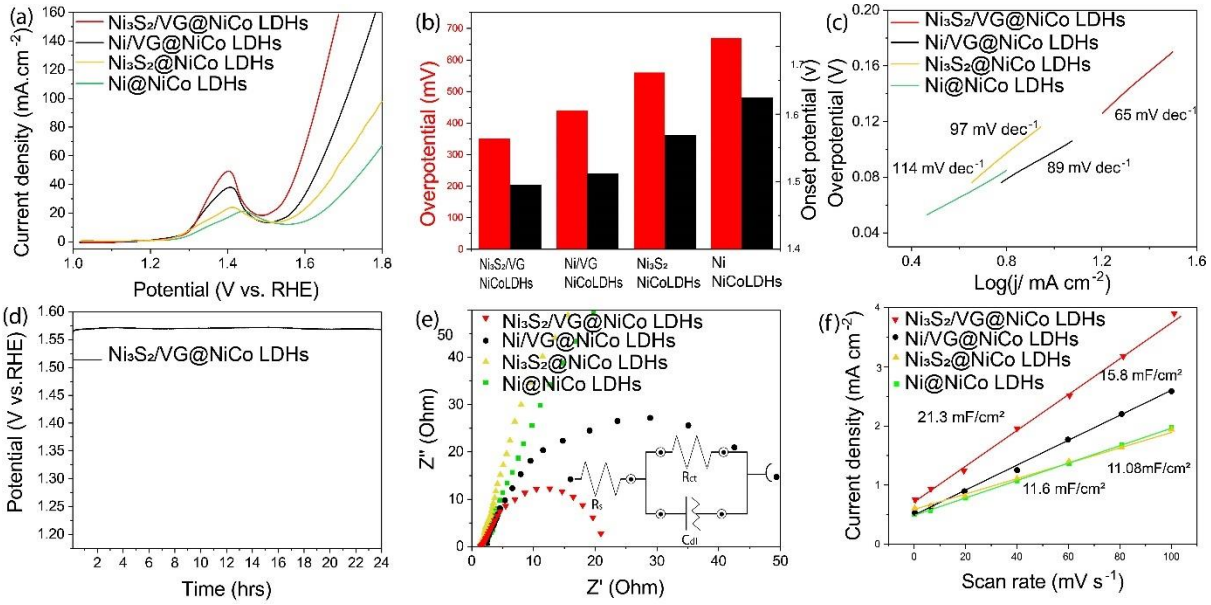

Fig. 4 (a) Linear sweep voltammograms (LSV) of Ni@NiCo LDHs, Ni/VG@NiCo LDHs, Ni_3S_2@NiCo LDHs and Ni_3S_2/VG@NiCo LDHs for OER. (b) Comparison of onset potential and overpotentials at a current density of 100 mA cm^{-2}. (c) The corresponding Tafel plots. (d) Chronopotentiometry curve of the Ni_3S_2/VG@NiCo LDHs at a current density of 20 mA cm^{-2} for 24 hours without iR correction. (e) Nyquist plots of Ni@NiCo LDHs, Ni/VG@NiCo LDHs, Ni_3S_2@NiCo LDHs and Ni_3S_2/VG@NiCo LDHs obtained at an overpotential of 300 mV. Inset shows the equivalent circuit. (f) The capacitive current density at a potential of 1.13 V vs RHE as a function of scan rate.

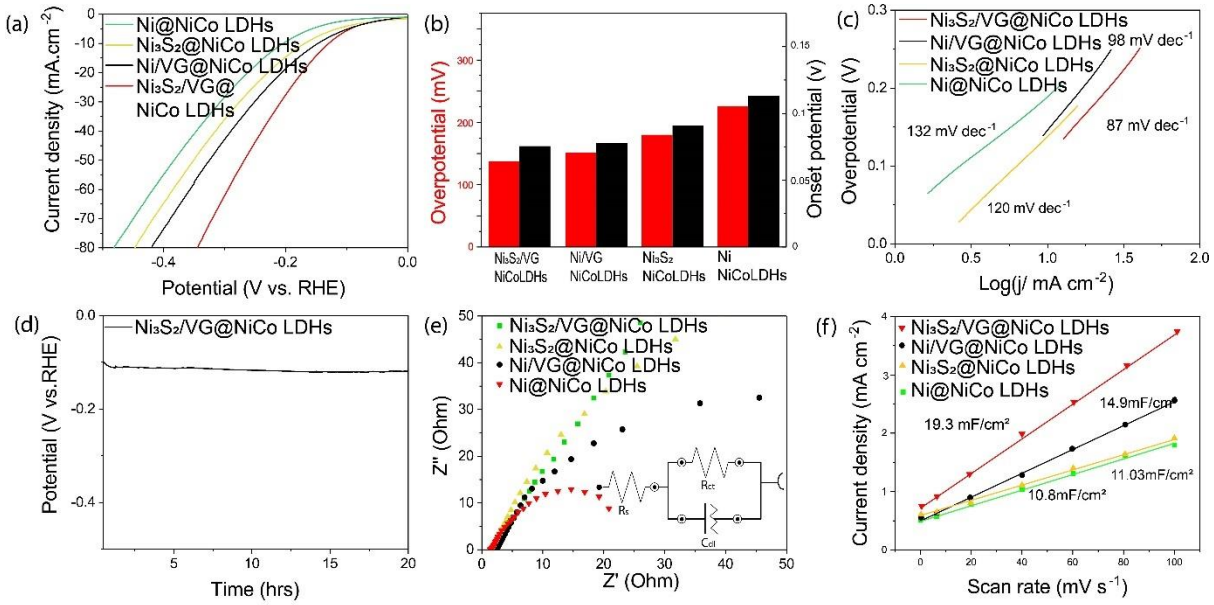

Fig. 5 (a) Linear sweep voltammograms (LSV) of Ni@NiCo LDHs, Ni/VG@NiCo LDHs, Ni_3S_2@NiCo LDHs and Ni_3S_2/VG@NiCo LDHs for HER. (b) Comparison of overpotentials and onset potentials at current densities 10 mA cm^{-2}. (c) The corresponding Tafel plots. (d) Chronopotentiometry curve of the Ni_3S_2/VG@NiCo LDHs at a current density of -10 mA cm^{-2} for 24 hours without iR correction. (e) Nyquist plots of Ni@NiCo LDHs, Ni/VG@NiCo LDHs, Ni_3S_2@NiCo LDHs and Ni_3S_2/VG@NiCo LDHs obtained at an overpotential of -150 mV. Inset shows the equivalent circuit. (f) The capacitive currents at a potential of 150 mV as a function of scan rates.

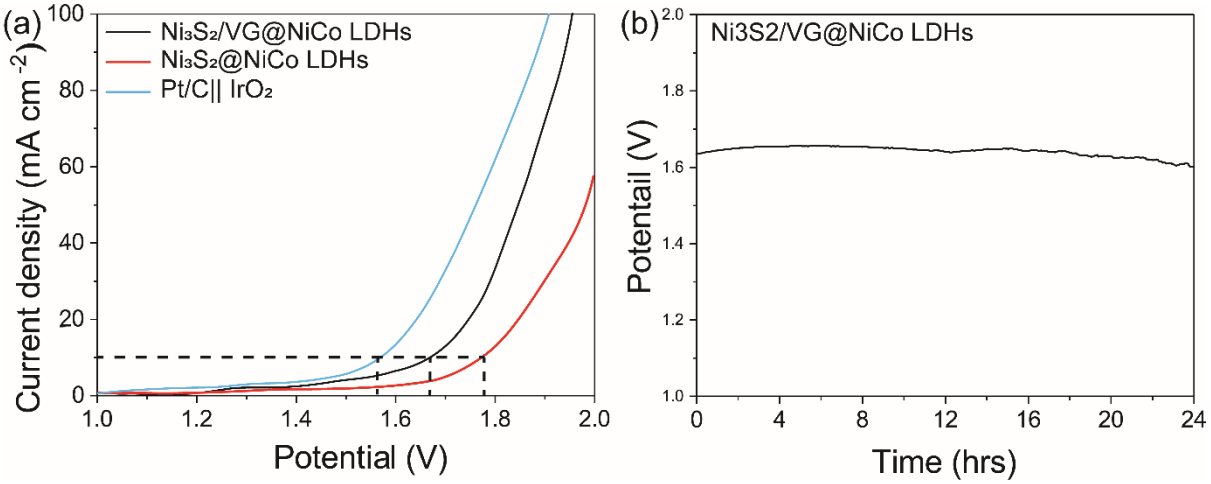

Fig. 6 (a) The polarization curves of water electrolysis for Ni_3S_2@NiCo LDHs, Ni_3S_2/VG@NiCo LDHs and Pt/C||IrO_2 at a scan rate of 5 mV s^{-1}. (b) Chronopotentiometry curve of overall water splitting using Ni_3S_2/VG@NiCo LDHs as the cathode and anode at a current density of 20 mA cm^{-2} for 24 hours.